

1 **Revision 1**

2
3 **Australian sedimentary opal-A and its associated minerals: Implications for natural silica**
4 **sphere formation**

5 Moritz Liesegang* and Ralf Milke

6 Institut für Geologische Wissenschaften, Freie Universität Berlin, Malteserstrasse 74-100, 12249

7 Berlin, Germany

8 *correspondence to: limo@zedat.fu-berlin.de

9 **ABSTRACT**

10 The vast majority of precious opal on the world market comes from opal fields in the Great
11 Artesian Basin of Australia pointing to very special prerequisites for amorphous silica to consolidate in
12 a way that leads to the famous play-of-color. We analyzed twenty opal-A samples from the Andamooka
13 (South Australia) and Yowah (Queensland) precious opal fields, using petrographic microscopy, XRPD,
14 SEM, and EPMA in order to identify and characterize opaline silica, the mineral assemblage, and the
15 host rock. Opal-A consists of submicrometer-sized silica spheres with an average diameter of 140-
16 320 nm. The average diameter of monodisperse spheres is 140-290 nm with a relative standard
17 deviation (RSD) of less than 6%. Polydisperse spheres show an average diameter of 160-320 nm with a
18 RSD larger than 10%. This dichotomy in size is reflected by the Na/K ratio at both localities.
19 Monodisperse spheres show values below 1.2 while polydisperse ones show a ratio larger than 3.0,
20 whereas other contaminations with higher valence show no correlations at all. We therefore suggest that
21 the jump in Na/K signals a fundamental change of pH and salinity of the silica-bearing mineralizing
22 fluids. Judging from the pH stability of the host rock minerals with predominating alunite, kaolinite,
23 illite and gypsum, and omnipresent barite and anatase we conclude that the dominant late-stage
24 mineralization leading to precious opal happened at acidic pH. Our findings indicate that the host rocks

25 and associated minerals are the key to unravel the complex history of opal-forming solutions. A
26 quantitative opal classification based on sphere diameters and their variability, decoupled from
27 gemological properties, is to be established.

28

29 **Keywords:** Opal-A, mineral chemistry, host rock, sphere size distribution, petrogenesis, Australia

30

31

INTRODUCTION

32 Opal-A is a non-crystalline form of hydrous silica ($\text{SiO}_2 \times n\text{H}_2\text{O}$) that often consists of
33 submicrometer-sized spheres. In precious opal-A, monodisperse spheres with a diameter of about
34 150-350 nm form a regular three-dimensional array that diffracts visible light, giving the characteristic
35 play-of-color (Jones et al. 1964; Sanders 1964), which is absent in common opal-A. However, there are
36 many factors that can suppress this optical effect in common opal, even if composed of monodisperse
37 spheres in regular arrangements, notably: sphere sizes too small or too large, strong cementation of
38 spheres, or an unsuitable contrast between the respective refractive indices of spheres and cement
39 (Sanders 1964; Darragh et al. 1966). A quantitative opal classification distinguishes between
40 monodisperse spheres and those with a broad sphere size distribution. While the synthesis of silica
41 colloids with a narrow sphere size distribution is among the better characterized processes in materials
42 science (e.g., Iler 1979; Xia et al. 2000; and references therein), the factors controlling sphere diameter
43 and dispersity in geological systems are still a matter of debate.

44 Precious opal-A at Andamooka (South Australia) and Yowah (Queensland) is associated with the
45 deeply weathered Early Cretaceous sediments of the Marree Subgroup and Winton Formation,
46 respectively (Senior et al. 1977; Barnes et al. 1992). From the Late Cretaceous to Early Miocene,
47 weathering of feldspar, mica, and clay minerals liberated silica into solution that migrated over short to
48 moderate distances (Darragh et al. 1966; Barnes et al. 1992). Silica-laden solutions were trapped within

49 about 40 m beneath the surface in voids, cracks and along groundwater permeability barriers e.g.,
50 kaolinitic sandstone overlying less permeable claystone. Slow evaporation gradually supersaturated
51 these trapped solutions, eventually leading to precipitation of amorphous silica and formation of
52 opal-A.

53 The precipitation of opal-A from solution is predominantly dependent on the degree of
54 supersaturation, ionic strength, and pH. At ambient conditions and $\text{pH} < 9$, the solubility of amorphous
55 silica is $\sim 100\text{-}150$ ppm, with a maximum at $\text{pH} 2\text{-}3$ and a minimum around 7 (Alexander et al. 1954;
56 Iler 1979). Electrolytes generally reduce the solubility, with polyvalent cations being more effective
57 than monovalent ones (Marshall and Warakowski 1980; Crerar et al. 1981). From supersaturated
58 solutions, particles grow by addition of silica monomers and polymers on the surface or by aggregation
59 with other solid particles (e.g., Bogush and Zukoski 1991; Icopini et al. 2005). Spheres in opal-A
60 consist of 25-40 nm-sized subparticles (Darragh et al. 1966; Jones and Segnit 1971; Gaillou et al.
61 2008b) and are most likely to form by an aggregative growth process. Experiments and modeling on
62 silica colloid formation from natural hydrothermal brine solutions show that particles with a diameter
63 of 30-40 nm are aggregates of nanoparticles ~ 3 nm in size (Icopini et al. 2005; Conrad et al. 2007).
64 These small particles have not been reported for natural opal so far. The surface properties of silica
65 particles are fundamental to colloid stability and strongly depend on solution pH and salinity. Above
66 the isoelectric point (IEP) at about $\text{pH} 2\text{-}3$, particles carry a negative surface charge that increases with
67 pH because of surface silanol dissociation. As a result, the colloid should be stable at high pH and
68 unstable at low pH, where spheres exhibit little or no surface charge. Silica particles smaller than a few
69 hundred nanometers act differently. They exhibit a local stability maximum at the IEP and a minimum
70 around $\text{pH} 6$ (Iler 1979; Kobayashi et al. 2005; Conrad et al. 2007). In electrolytes, counter-ions
71 accumulate close to the negatively charged particle surface and form a diffuse electrical double-layer
72 whose extent $1/\kappa$ is inversely proportional to the square root of the ionic strength. When particles
73 approach, their double-layers overlap and repulse each other.

74 On the basis of pH and salinity, Stewart et al. (2010) calculated, that monodisperse spheres, as in
75 opal-A, self-assemble by electrostatic forces into an ordered array at pH 9-10 and $c_{\text{NaCl}} 10^{-3}$ - 10^{-4} M.
76 This result contradicts the assumption of opal formation at neutral to mildly acidic pH and the common
77 opinion of gravity-driven sorting of slowly sedimenting uniform spheres (Iler 1965; Darragh et al.
78 1966; Gaillou et al. 2008b). In contrast, Piret and Su (2008) synthesized self-assembled arrays of
79 monodisperse silica spheres from tetraethylorthosilicate at pH 1-3 and 10 with $c_{\text{NaCl}} 10^{-2}$ - 5×10^{-2} M.
80 Noting the difference between calculations and experiments, clarification of the relevant solution
81 characteristics is needed to understand natural opal formation. The parent solutions of the two types of
82 Australian opal are unknown, and their properties and qualities can only be deduced from indirect
83 observations such as the assemblage of coexisting minerals and their stability depending on pH and
84 solution composition. We investigate the relation between sphere size distribution and chemical
85 composition of natural opal. This is a further step towards a better understanding of opal formation in a
86 sedimentary setting.

87

88

MATERIALS AND ANALYTICAL METHODS

89 **Sample origin and acquisition**

90 Sixteen samples from Andamooka (South Australia) and four samples from Yowah (Queensland)
91 were investigated using a number of methods, in order to identify and characterize opaline silica, the
92 mineral assemblage, and the host rock (Table 1). Samples were collected in the Teatree Flat field
93 located about 15 km northwest of the Andamooka Township and from different locations within the
94 Yowah opal field located a few kilometers south of the town of Yowah. All samples were transported in
95 sealed polyethylene bags until further preparation. The host rock and silicified samples from
96 Andamooka were extracted from bulldozer cuts about 20 m beneath the surface, in close proximity to
97 the layer (named “level” by the miners) in which most precious opal is found. Silicified samples from
98 Andamooka consist of sediments (mudstones, conglomerates, an opal breccia, and a silicified pebble),

99 mollusc shell pseudomorphs, and coniferous wood (Fig. 1). Samples from Yowah are spherical
100 siliceous ironstone nodules. Opals analyzed include gray, white, light brown, colorless, and transparent
101 honey-colored samples. All specimens were stored in sealed polyethylene boxes between analyses to
102 prevent exsiccation. Procedures for sample and specimen preparation are described in detail below.

103 **Thin section preparation and optical petrography**

104 Opals and silicified sediments were cut using a 10" diamond-impregnated steel lapidary saw,
105 which was cooled by tap water. Friable porous samples were cut using a 5" diamond-impregnated steel
106 lapidary saw cooled with water-free Isocut Fluid (Buehler). These specimens were subsequently rinsed
107 with acetone to remove debris and cut fluid, dried overnight in an oven at 35 °C and embedded in
108 epoxy resin prior to lapping and finishing. Polished thin sections of standard dimensions (~26×48 mm
109 at ~30 µm thickness) were prepared using standard procedures. Specimens were cleaned between
110 subsequent preparation steps by ultrasonication, to remove debris and relic abrasive. Sections were
111 thinned to the required thickness with SiC 800-1200 powder, then on bonded diamond laps, and
112 finalized with diamond paste down to 0.25 µm. Polished sections were studied using polarizing optical
113 microscopy with magnifications ranging from 35-400×. Locations without visible mineral inclusions
114 and/or underlying grains were pre-selected for later electron probe microanalysis. Most minerals in the
115 studied samples were too small for optical identification and were identified by EPMA.

116 **Scanning electron microscopy - SEM**

117 The surfaces of etched and unetched fractures freshly produced in the laboratory were imaged by
118 SEM. Specimens were vapor-etched over 40 vol% HF solution for 20 s and dried afterwards. Stub-
119 mounted etched and unetched specimens were sputter-coated with ~15 nm W. Secondary electron
120 images were obtained in a Zeiss Supra 40 VP Ultra SEM instrument, operated at 10⁻³ Pa vacuum
121 chamber pressure, acceleration voltage 10 kV at a beam current of 10 nA. With current settings,
122 instrument resolution was about 2 nm, whereas opal sphere diameters range from ~100-600 nm. For

123 each specimen, observed spheres were traced manually before being processed digitally with ImageJ
124 software (Abràmoff et al. 2004). Average sphere diameters were calculated from the computerized data
125 of four-hundred particles.

126 **Electron probe microanalysis - EPMA**

127 Polished thin sections were prepared for analysis by sputter coating with ~20 nm carbon to prevent
128 charging. Quantitative element concentrations were determined using a JEOL JXA 8200 Superprobe.
129 Chamber vacuum was at 3×10^{-2} Pa or better. The instrument was operated at 15 kV acceleration voltage
130 and 20 nA beam current (on Faraday cup). During measurements, the beam diameter at the point of
131 incidence was focused to 1 μm . We measured opal compositions at different beam diameters (1-20 μm),
132 15 kV, and 20 nA, in 10 spots randomly distributed over some specimens to assess the effect of areal
133 current density on element migration (especially Na) and measurement validity. Compositions obtained
134 at these conditions did not vary systematically or significantly, showing that EPMA at small beam
135 diameters should be applicable to analyze opal, but is obviously limited by the respective lower limit of
136 detection (LLD) of the measured elements. Automated and manual measurements of opals were
137 alternated with measurements of internal standard reference materials (e.g., feldspar, quartz) to identify
138 systematic errors. At least one-hundred point analyses were acquired from each opal specimen.
139 Acquisition time for each Na analysis was set to 5 s on peak and 5 s on background. Peak and
140 background of other elements were measured for 10 s each. X-ray signal was recorded on five WDS
141 detectors (LIFH, PETH, PETJ, 2×TAP). Sodium and potassium were both allocated to a separate WDS
142 detector. Sodium and aluminum were counted first, while silicon and potassium were counted in the
143 second run, as suggested by Morgan and London (2005). The instrument was internally calibrated
144 using synthetic/natural silicate, oxide, sulfate, and REE-phosphate standards. During measurements,
145 the acceleration voltage and beam current were identical to the standardization conditions for all
146 elements. With the above analytical setup, resulting net lower limits of detection were at around

147 0.01 wt% for most elements, but around 0.03 wt% for Na₂O. Raw data were corrected using the ZAF
148 algorithm and are presented as element oxides, notably Na₂O, K₂O, MgO, CaO, SrO, BaO, MnO,
149 Al₂O₃, Fe₂O₃-total, TiO₂, and SiO₂. Given its abundance, absolute analytical error for SiO₂ is around
150 0.50 wt%. Water contents were calculated as the difference between the measured total and 100.00
151 wt%. These values are directly influenced by the analytical errors in the element species actually
152 measured. Repeated analyses of opals over a 3.5-year period revealed no increase of the measured total.
153 Therefore, desiccation of the specimens in SEM/EPMA vacuum seems negligible. Elemental maps
154 were made using the WDS detectors. Operating conditions were 15 kV accelerating voltage and 20 nA
155 beam current (on Faraday cup), with a beam diameter of 1 μm and 60 ms counting time per 0.5-1 μm
156 pixel size.

157 **X-ray powder diffraction - XRPD**

158 A number of sub-samples were prepared from counterparts of thin-sectioned material, hand-picked
159 under a stereo microscope and pre-crushed in an agate mortar to pass a 325-mesh (44 μm openings)
160 sieve. About 5 g of pre-crushed material was then charged into a ball mill equipped with a stainless
161 hardened steel ball and ground under acetone for 10 min at low rotor speeds to an average particle size
162 of approximately 5 to 20 μm. The slurry was poured out into a Petri dish and the grinding jar rinsed
163 with acetone to transfer all material. Specimens were covered and allowed to dry overnight in an oven
164 at 35 °C, after which the dried powder was homogenized and stored in a polyethylene vial. For X-ray
165 analysis, about 0.5 g of prepared powder was mounted in a specimen holder by side-loading to
166 minimize preferred orientation. For specimens containing quartz, the position of the (101) peak was
167 used as an internal standard. Opals and the quartz-free Yowah samples were measured in an aluminum
168 specimen holder ($a=4.0496 \text{ \AA}$) so that the diffractograms could be calibrated. Diffractograms were
169 recorded 6-65 °2θ on a PDF-2 X-ray instrument from EFG GmbH Berlin operated at 40 kV and 20 mA,
170 producing non-monochromated Ni-filtered CuKα radiation with $\lambda=1.541718 \text{ \AA}$. Step size was set to

171 0.04 °2 θ at 4 s acquisition time per step. Modal mineral contents were determined from full-profile
172 analysis using the Match 1.11f software package (Crystal Impact GbR, Bonn, Germany). Lower
173 detection limits were ~1-2 vol%.

174

175

RESULTS

176 **Petrographic description of silicified samples**

177 The silicified sediments from Andamooka investigated here consist of silty mudstones,
178 conglomerates, an opal breccia, and a silicified pebble. Opal-replaced materials include gray and
179 translucent white mollusc shell pseudomorphs, and coniferous wood. A friable coating of
180 unconsolidated mud on the surface indicates selective silicification. The majority of opal-bearing
181 sediments are intensely opal-cemented, resulting in a very low porosity of the consolidated product.
182 Opal-cemented, silty mudstones contain some light brown to gray, well-rounded, flat or elongate
183 argillaceous siltstone and shale lithoclasts up to 8 mm long in an almost white to light grayish-brown
184 matrix. The matrix mainly consists of kaolinite books, detrital sub-rounded quartz, and minor lath-like
185 illite. Light brownish opal-A partially replaced the clay matrix without preserving original structures.
186 Colorless and transparent honey-colored opal-A intrudes the matrix and light brownish opal and is
187 parallel to subparallel to the primary bedding direction (Fig. 2a).

188 Opal-cemented conglomerates consist of light gray to brown, poorly sorted, well-rounded,
189 elongated quartz-arenite and quartzite lithoclasts up to 20 mm long in a pale red to gray kaolinitic
190 matrix with sand-sized, sub-rounded to well rounded quartz, and trace amounts of illite. The grain-
191 supported microquartz-cemented opal breccia contains highly angular, 2-40 mm large, light yellow and
192 brown clasts with abundant weakly birefringent domains and occasional veins of transparent opal-A
193 with intense play-of-color (POC). Clast surfaces are often covered by water-clear botryoidal amorphous
194 silica. X-ray diffraction patterns of whole rock samples indicate a mixture of quartz and opal-CT (see
195 XRPD section). Weakly birefringent domains inside the clasts contain some chalcedony. Some of the

196 clasts also contain concentrically zoned, round to ellipsoidal ooid structures that rarely exceed 300 μm
197 in size. The ooids are deformed when in contact with authigenic K-feldspar grains. Another sample rich
198 in microstructural features is the gray, ~60 mm large, silicified pebble (Table 1). It is composed of
199 quartz, traces of transparent to translucent hydrous silica phases, and very few, minute-sized (2-10 μm)
200 illite and barite grains. Some rounded pores contain transparent opal-A with intense blue to green POC.
201 Rhombohedral pseudomorphs are widespread in this sample and consist of euhedral quartz grains
202 ranging from 10-30 μm in size. The pseudomorphs contain small cavities frequently lined with
203 translucent white, weakly birefringent, botryoidal aggregates <20 μm across (Fig. 2b). Coniferous
204 wood with well-preserved tracheids and bordered pits consists of white to light brownish common
205 opal-A. Veins developed perpendicular to the rays are filled with colorless to transparent honey-colored
206 opal-A and occasionally contain loose fragments with tracheid structures. Mollusc shell pseudomorphs
207 consist of either translucent white or gray opal-A with a vivid blue to red POC.

208 Spherical, concentric zoned, dark-brown limonite concretions from Yowah range from 2-8 cm
209 across. Whole rock XRPD analyses reveal the abundant presence of goethite and to a minor extent
210 hematite, kaolinite, and illite. Dark-brown goethite/hematite layers alternate irregularly with light-
211 brown clay mineral layers and opal-A veins. The clay mineral bands, that are tens to hundreds of
212 micrometers wide, coat the surface of voids and are composed of kaolinite, illite, anatase, and a number
213 of aluminum-phosphate-sulfate (APS) minerals. Opal-A fills pseudomorphs after rhombic elongated
214 minerals - possibly gypsum or feldspar - and the network of thin concentric and radial fractures inside
215 the ironstone nodules. Opal-A in veins is transparent and predominantly displays a strong POC that
216 spans the entire visible spectrum. A fine parallel striation in vein opals is common among the Yowah
217 samples and infrequently extends into the narrow vein ends. The rhombic pseudomorphs (Fig. 2c),
218 frequently up to 1.5 mm long with cracks (<20 μm) developed perpendicular to the longest axis, often
219 form aggregates and fan-like arrangements in the goethite groundmass. They contain transparent
220 opal-A with an intense violet-blue POC.

221 Generally, opal-A fills millimeter to centimeter wide voids and cracks in silicified sediments.
222 Precious opals have a gray, colorless transparent or rarely translucent white body color. Common opals
223 are white, light brown, colorless, or transparent honey-colored. Colorless and transparent honey-
224 colored opals usually do not display a POC except for a few scattered millimeter-sized faint violet to
225 blue domains. Some common opals therefore resemble low-quality precious opal-A. Precious and
226 common opals frequently display $<30\ \mu\text{m}$ wide, polygonal desiccation cracks (Fig. 2d). The cracks in
227 precious opals remain open, while those in white and light brown common opals often contain
228 authigenic illite, kaolinite, and occasionally some minute-sized (hundred nanometer) barite, anatase, or
229 gypsum crystallites. Neither cracks nor inclusions are visible with the unaided eye in hand-specimen. In
230 many samples, we observed that large cracks ($>50\ \mu\text{m}$) and millimeter-long faults in white to light
231 brown common opal are filled with colorless or transparent honey-colored opal-A, which sporadically
232 displays a faint violet POC.

233 **The Andamooka host rock and opal-associated minerals**

234 The unsilicified friable host rock at Andamooka is an extensively bleached, white to light-yellow,
235 iron stained mudstone without evidence of bedding. X-ray diffraction analyses of whole rock samples
236 reveal a modal mineral content (in vol%) of about 50% kaolinite, 35% quartz, 10% alunite, and minor
237 amounts of illite, hematite, anatase, and barite, which is consistent with optical inspection of thin
238 sections and X-ray mapping. The rock predominantly consists of kaolinite particles $<2\ \mu\text{m}$,
239 homogeneously distributed kaolinite books, and silt-sized intense corroded quartz grains (Fig. 3a). This
240 rock is characterized by large (up to $200\ \mu\text{m}$) randomly distributed pockets throughout the sediment.
241 These are filled with colorless, micrometer-sized, pseudocubic alunite crystals. In the clay matrix,
242 kaolinite particles ($<2\ \mu\text{m}$) are closely associated and replaced by alunite crystals up to $5\ \mu\text{m}$.

243 The main minerals in silicified samples from Andamooka are kaolinite and quartz. Kaolinite
244 usually occurs as a fine-grained, gray to brown mass composed of clay-sized particles. Throughout the

245 kaolinitic groundmass, rare vermicular kaolinite books and lath-like illite particles are scattered
246 irregularly. Blocky kaolinite aggregates can reach a size of 200 μm , whereas illite particles are often
247 $<20 \mu\text{m}$ and rarely exceed 100 μm in size. Replacement of illite by kaolinite is widespread and appears
248 in the form of up to 10 μm thick kaolinitized lamellae parallel to the direction of elongation (Fig. 3b).
249 Microprobe analyses and X-ray mappings of clay-rich areas indicate that considerable amounts of
250 xenomorphic anatase, barite, and hematite grains $<5 \mu\text{m}$ are present as impurities. Detrital quartz grains
251 are commonly sub-angular to rounded and intensely fractured. Authigenic quartz frequently displays
252 corrosion pitting covered by botryoidal amorphous silica. In places, zoned, intensely corroded, tabular
253 barite grains ($<100 \mu\text{m}$) are accumulated on the surface of fracture-coating botryoidal silica. Gypsum
254 particles ($<2 \mu\text{m}$) with granular appearances are developed exclusively in cracks within opal-A.

255 Pores in silicified sediments contain alunite crystals that are predominantly smaller ($<3 \mu\text{m}$) than
256 those in the host rock. The alunite-containing pores are often surrounded by transparent opal-A. Where
257 present, alunite normally occurs in association with clay-sized kaolinite particles, and occasionally with
258 barite and K-feldspar. Euhedral, elongated K-feldspar crystals occur as transparent grains $<200 \mu\text{m}$ in
259 size, some of which have prominent parallel dissolution channels along the c-axis (Fig. 3c). Pores filled
260 with K-feldspar may contain barite in the form of euhedral tabular grains and concretionary masses. In
261 one sample, it was observed that several pores contained partially dissolved K-feldspar and massive
262 barite with embedded pseudocubic alunite. Chalcedony is a trace constituent within breccia clasts, and
263 is virtually absent from other samples. In rock thin sections chalcedony occurs as translucent white,
264 length-fast, spherulitic and rarely as a wall-lining filling of isolated pores and veins $<200 \mu\text{m}$.
265 Gorceixite and members of the gorceixite-florencite-(Ce) solid-solution series have been identified by
266 EPMA as very rare, minor constituent in the opal breccia from Andamooka. Gorceixite occurs in
267 euhedral, up to 50 μm large, transparent crystals. Gorceixite-florencite-(Ce) forms $\sim 30 \mu\text{m}$ thick rims
268 lining pores left by grain dissolution. The rims display a patchy and broad growth zonation when
269 viewed under backscattered electron (BSE) imaging (Fig. 3d). Submicrometer-sized APS crystals in

270 this sample occur in clay-rich bands lining detrital quartz surfaces. Goethite in the Yowah rock samples
271 typically forms aggregates (<4 μm) of acicular crystals, with blackish to reddish brown color in thin
272 section. Less frequently, reniform aggregates with radial structure line opal-filled veins. APS minerals
273 in the Yowah samples often are stubby six-sided, <3 μm large grains confined to clay layers.

274 **SEM observations on opals**

275 Opal-A from both sample localities consists of spheres with variable size, ordering, internal
276 structure, and degree of cementation (Fig. 4a-d). Figure 5 shows that spheres of different diameter are
277 grouped into monodisperse or polydisperse ones. Colorless and transparent honey-colored common
278 opals as well as transparent, translucent white, and gray precious opals consist of regularly arranged
279 monodisperse spheres. The average diameter of monodisperse spheres ranges from 140-290 nm with a
280 relative standard deviation (RSD) between 3.8-6.0%. White and light brown common opals consist of
281 irregularly arranged, polydisperse, round to ellipsoidal spheres with an average diameter of 160-
282 320 nm and a RSD between 10.6 and 15.6%. A smooth thin layer of silica often coats coalesced
283 spheres. Mollusc shell pseudomorphs consist of well-ordered monodisperse spheres with an average
284 diameter of 210-260 nm. In part, deformation of one shell sample resulted in hexagonal sphere cross-
285 sections. Deformed, elongated to ellipsoidal spheres in the Yowah samples often display up to three
286 unfilled cores. The deformed spheres occur in <5 μm wide veins and along the surface of >100 μm
287 wide goethite-lined veins filled with uniformly sized spheres. The degree of sphere deformation in wide
288 veins increases from the vein interior towards the goethite margin. After HF etching, spheres in void-
289 filling common and precious opals often display a central 20-50 nm-sized nucleus or central depression
290 surrounded by up to two concentric shells. Opals differ by the degree to which the interstices between
291 spheres are filled with silica cement. For example, spheres in mollusc shell pseudomorphs with a vivid
292 POC contain considerably less cement than those in void-filling opals without a POC. This feature is
293 especially pronounced in unetched specimens.

294 Morphological changes of opaline phases inside partly dissolved rhombohedral pseudomorphs in
295 the silicified pebble were captured by SEM images (Fig. 4e, f). These revealed micro- to nano-sized
296 particle changes within a distance of a few hundred micrometers. Each pore coating in the
297 pseudomorphs contains silica particles of individual size and morphology. The particles are in direct
298 contact with the underlying quartz substrate and have a microstructure of interpenetrating blades
299 similar to those observed in siliceous sinter modified by progressive diagenetic overprint (Lynne et al.
300 2005). We observed two textural features that have been described as poorly bladed and well-bladed
301 opal-CT lepispheres (Flörke et al. 1976). Well-bladed lepispheres are either round, up to 1.8 μm across,
302 and consist of well defined ~ 50 nm thick blades with smooth edges, or form cauliflower-like
303 aggregates of coalescent lepispheres (5 to over 20 μm across) with ~ 60 nm thick platelets and jagged
304 edges. Poorly bladed lepispheres are ellipsoidal, up to 1.5 μm large aggregates of ~ 120 nm thick
305 platelets with jagged edges. The jagged edges of lepisphere platelets resemble aligned 60-120 nm large
306 silica nanospheres.

307 **EPMA analysis of opals and associated minerals**

308 Impurities of all opal-A samples are Al_2O_3 , Fe_2O_3 , CaO , Na_2O , K_2O , MgO , and BaO . All
309 impurities but Al_2O_3 and CaO appear in trace amounts <0.1 wt%. A typical location for electron probe
310 microanalysis on polished thin sections is shown in Figure 6. Representative analyses of opals are
311 presented in Table 2. Water contents ($\text{H}_2\text{O} + \text{OH}$), calculated by balance with 100.00 wt%, range
312 between 4.00 and 8.20 wt%. The sum of cation impurities does not exceed 2.39 wt% and in most cases
313 is below 1.45 wt%. No co-variation is observed between the total impurity level and the visual
314 appearance of opals. Sodium and potassium account for less than 20% of the impurity concentration.
315 SrO , MgO , MnO , and TiO_2 contents are generally low ($<\text{LLD}$ to 0.03 wt%) and do not vary
316 systematically. While BaO contents mostly range from 0.01-0.03 wt%, relative BaO enrichment (0.07-
317 0.09 wt%) is observed in void-filling white and transparent opal of one conglomerate sample. It is

318 evident that the Al content between adjacent common/precious and different-colored common opals
319 does not vary significantly (<10%). Significant variations in Al and Ca content are recorded between
320 void-filling opals (0.75-1.21 wt% Al₂O₃; 0.04-0.11 wt% CaO) and mollusc shell pseudomorphs (1.31-
321 1.53 wt% Al₂O₃; 0.27-0.40 wt% CaO). Fe₂O₃ is less abundant in Andamooka opal (up to 60% less)
322 than in Yowah vein opal. Yowah opal-A in rhombic pseudomorphs and veins shows similar trace
323 element profiles. Only Fe₂O₃ varies significantly from about 0.03 wt% in the pseudomorphs to
324 0.21 wt% in veins.

325 The main difference in the geochemical characteristics of all studied opals is their Na/K ratio.
326 From Figure 7, it is evident that the sphere size distribution of opal-A in voids and pseudomorphs
327 varies with the Na/K ratio. Monodisperse spheres display a narrow range of values <1.2, while
328 polydisperse spheres have variable ratios >3.0. In contrast to Na/K, the sum of Na and K, which is
329 0.07 wt% on average, allows no distinction between spheres of different size distribution. The Na + K
330 of monodisperse spheres scatters from 0.03 to 0.13 wt%, while polydisperse ones have concentrations
331 from 0.05 to 0.12 wt%.

332 Several minerals are associated with opal-A such as kaolinite, illite, and K-feldspar. Their
333 compositions are collated in Table 3. Microprobe data show that the illite from both deposits is
334 predominantly a K-rich variety, low in Mg and Fe. The chemical composition of kaolinite and illite
335 remains uniform throughout each rock sample but varies slightly between Andamooka and Yowah
336 samples. The relatively iron-enriched opals from the Yowah samples coexist with kaolinite and illite
337 that contain ~50 and ~80% more Fe₂O₃ respectively. The goethite formed in Yowah ironstone nodules
338 has an average Al substitution of <3 mol% estimated from the position of the 110 (4.185 Å), 111
339 (2.449 Å), and 130 (2.697 Å) diffraction lines (Fitzpatrick and Schwertmann 1982; Schulze 1984). This
340 value agrees well with EPMA data that indicate an average Al substitution of ~1.6 mol%. Based upon
341 probe analyses, K-feldspar compositions range from Or₉₁ to Or₉₉ in the Andamooka samples and from
342 Or₉₂ to Or₉₅ in the Yowah samples.

343 APS minerals (for review see Dill 2001) have been identified in silicified sediments and the
344 Andamooka host rock. The unit-cell dimensions a (6.98 Å) and c (17.32 Å), calculated from XRPD
345 measurements, indicate that alunite in the Andamooka host rock is a K-rich member of the
346 alunite/natroalunite solid-solution series (compared to peak positions from Parker 1962). EPMA
347 analysis shows that alunite in the Andamooka host rock has a molar $K/Na > 13$, whereas silicified rocks
348 contain alunite with a molar K/Na of 5-9. The amount of BaO in the host rock alunite is considerably
349 lower than in alunite from silicified sediments (0.13 and 3.64 wt% respectively). Conversely, alunite in
350 the host rock contains more K_2O than alunite in silicified sediments (10.13 and 7.94 wt% respectively).

351 Other APS minerals identified in an Andamooka sample are gorceixite and members of the
352 gorceixite-florencite-(Ce) solid-solution series. Gorceixite crystals have homogenous compositions and
353 show minor substitution of Ba by Ca and Ce, with a molar $Ba/(Ca + Ce) > 6.2$. Gorceixite-florencite-
354 (Ce) crystals display compositional zoning because of Ba-Ce substitution. Their molar $Ba/LREE$ is
355 > 1.5 , with up to 9.07 wt% $LREE_2O_3$ (sum of La, Ce, Pr, and Nd oxides). APS minerals from the Yowah
356 field have heterogeneous and complex compositions, with variable amounts of K, Sr, Ba, and Ca. The
357 APS minerals might be described as potassian goyazite, but their composition could only be obtained
358 from $< 3 \mu m$ large crystals, making it difficult to provide an accurate classification. The molar P/S ratio
359 of APS minerals (except alunite) from Andamooka is > 25 , while those from Yowah have a ratio < 2 .
360 The molar Al/Fe^{3+} of these minerals from Andamooka is > 15 , while those from Yowah have a ratio < 4 .

361 **Opal X-ray diffraction data**

362 The typical XRPD patterns of opal phases in the samples studied are shown in Figure 8.
363 Diffractograms of opal-A are characterized by a major broad asymmetric reflection located at 4.004 Å
364 (22.2 °2 θ) on average. The position of the main peak varies from 3.995 to 4.015 Å (22.25 to 22.14 °2 θ)
365 between individual samples. The full width at half maximum (FWHM) of this peak ranges from
366 6.75-7.51 °2 θ . An additional very broad reflection of low intensity with a maximum at 1.95-2.01 Å

367 (46.54-45.06 °2θ) is observed in about half of the diffractograms. We found no co-variation between
368 peak shape/position and the visual appearance, micromorphology, or chemical aspects of opal-A. The
369 XRPD pattern of the opal breccia shows characteristic quartz peaks and a prominent reflection centered
370 at 4.101 Å (21.67 °2θ) with a FWHM of 0.96 °2θ and a slight shoulder on the high-°2θ side. The
371 position of this peak corresponds most closely to the d-value of α-tridymite *hkl* (-404) (Flörke 1955) at
372 4.107 Å (21.6 °2θ). An additional peak of lower intensity is located at ~2.50 Å (35.94 °2θ). According
373 to the Jones and Segnit (1971) classification scheme the peak shapes/positions are consistent with
374 opal-CT. The diffractogram lacks additional cristobalite-related peaks (e.g., Ghisoli et al. 2010)
375 between 3.14 Å (28.5 °2θ) and 2.84 Å (31.5 °2θ). A minor contribution of opal-A to the diffraction
376 pattern cannot be excluded.

377

378 DISCUSSION

379 **Geochemical features of opal-A**

380 Petrographic and mineralogical analyses indicate that opal-A is the main silica phase in the
381 silicified sediments from Andamooka and Yowah. Microprobe analyses of 20 opals yielded data for 10
382 cation impurities in amorphous silica spheres. The results show that the composition of common and
383 precious opal-A is highly variable. Seemingly, opalized mollusc shell pseudomorphs partially preserved
384 the Ca-rich composition of the parent material. Yowah opal composition data are absent from literature,
385 but to our knowledge there are three chemistry studies on void-filling opal-A clearly assigned to the
386 Andamooka opal field (Bayliss and Males 1965; Brown et al. 2004; Gaillou et al 2008a) to which we
387 can compare our data. However, some literature data lacks relevant elements such as K and Ba (Bayliss
388 and Males 1965) and Ba (Brown et al. 2004). The majority of Andamooka opal in the present study
389 contains fewer impurities, specifically K, Ca, and Al, than those mentioned in the literature.
390 Compositional variations may arise from the amount of water and additional substitution of Si⁴⁺ by Al³⁺
391 or Fe³⁺, which is compensated by the incorporation of mono- and divalent cations and OH groups

392 (Webb and Finlayson 1987; Gaillou et al. 2008a). The positive correlation between the sum of trivalent
393 cations (Al^{3+} , Fe^{3+}) and mono- and divalent cations (Na^+ , K^+ , Mg^{2+} , Ca^{2+} , Ba^{2+}) in Andamooka and
394 Yowah opal-A illustrates such a relationship (Fig. 9). This relation indicates that cations are structurally
395 incorporated into growing spheres and do not accumulate solely on the particle surface.

396 Some authors noted that precious opal-A has a more constant impurity concentration than common
397 opal-A (e.g., Gaillou et al. 2008a). In contrast, others reported that precious and common opals show
398 very similar trace element profiles (Bayliss and Males 1965; McOrist and Smallwood 1997; Brown et
399 al. 2004). Our results do not reveal a relation between the sum of impurities and the opal-A variety. In
400 fact, opals composed of monodisperse spheres, regardless of their gemological classification, tend to
401 have less constant element concentrations than opals composed of polydisperse spheres. This result
402 cautions against the gemological distinction between common and precious opal as a primary
403 determinative tool.

404 Compositional variations could also be related to microscopic structures observed in opal-A. Thin
405 section petrographic analysis revealed that $<30\ \mu\text{m}$ wide cracks in white and light brown common
406 opal-A often contain illite, kaolinite, barite, anatase or gypsum. Clay-related elements such as Na, K,
407 Ca, Mg, and Al also represent the major opal impurities. Slight admixture of mineral impurities in
408 cracks may shift the measured cation content of bulk opal samples towards higher values, hardly
409 recognizable by comparison of mono- and polyvalent cations. These impurities represent a significant
410 factor for composition-based interpretations. Therefore, caution must be exercised when analyzing bulk
411 samples because subtle but significant mineral inclusions may be overlooked.

412 **Relation between the opal-A Na/K ratio and silica sphere properties**

413 We have identified that monodisperse and polydisperse spheres in Andamooka and Yowah opal are
414 separated by their Na/K ratio, restricting the appearance of monodisperse spheres to values <1.2 and
415 polydisperse spheres to values >3.0 . Interestingly, this relation includes void-filling opal-A and

416 pseudomorphs, which most likely formed by different mechanisms. Other trace elements do not appear
417 to correlate with the silica sphere micromorphology in the present study. This relation is surprising,
418 considering the low concentration of monovalent cations. Some researchers suggest that polydisperse
419 spheres sediment from thicker, more concentrated solutions than monodisperse spheres (e.g., Darragh
420 et al. 1966; Gaillou et al. 2008b). Accordingly, slow sphere growth and sedimentation are considered a
421 prerequisite for precious opal formation. Spheres can grow by aggregation of subparticles, as indicated
422 by SEM observations on natural opal-A (Darragh et al. 1966; Gaillou et al. 2008b) and experiments
423 (e.g., Conrad et al. 2007). Electrolytes increase the polymerization of silica in solution and accelerate
424 the aggregation and subsequent sedimentation of silica spheres. K reduces the repulsive interparticle
425 forces more effectively than Na (Sonnefeld et al. 1995; Dove and Craven 2005), which suggests that
426 unstable, polydisperse spheres could have a low Na/K fingerprint. This contrasts with our observation
427 of monodisperse spheres with a lower Na/K ratio than polydisperse spheres.

428 Although monovalent cations modify the solubility and surface properties of amorphous silica,
429 polyvalent cations are more efficient at reducing the amorphous silica solubility and screening length of
430 the electrical double-layer around charged silica particles (e.g., Marshall and Warakomski 1980;
431 Wijnen et al. 1993; Dove and Craven 2005). Deduction of opal formation mechanisms from its
432 monovalent cation fingerprint alone seems insufficient, as polyvalent cations, anions, and pH may play
433 a more significant role in silica colloid behavior. Based on these considerations, it appears unlikely that
434 Na and K control sphere size distribution, despite the correlation of Na/K ratio and dispersity. The
435 absence of this relation implies that other parameters such as pH and salinity, which cannot be derived
436 directly from the opal composition, may play a more important role in opal formation.

437 **Opal-associated minerals - implications for opal-forming solutions**

438 We suggest that the Na/K ratio represents significant differences in the overall solution
439 characteristics. The spatial, and therefore temporal, relation of opal with monodisperse spheres

440 intruding opal with polydisperse spheres illustrates this major change. It is important to note that the
441 opposite case was never observed. The high Na/K of polydisperse spheres may mark a solution
442 composition triggered by hydrolysis of Na-rich minerals. The absence of such minerals from the
443 samples and the low Na/K of uniform spheres could imply that there was sodium removal from
444 solution. Alternatively, sodium phases could have been unstable in the opal-bearing rocks. The solution
445 composition changed after the precipitation of polydisperse spheres, along with deformation and
446 cracking probably induced by dehydration or small-scale faulting. Such dehydration events are
447 consistent with a fluctuating groundwater table due to an arid climate, which is considered essential for
448 opal formation at the Australian fields (Darragh et al. 1966; Senior et al. 1977; Barnes et al. 1992).
449 Silica liberation at opal fields is commonly attributed to the kaolinitization of feldspar, mica, and clay
450 minerals at neutral to acidic pH. These reactions provide K^+ and Ba^{2+} , components that are essential for
451 the authigenesis of alunite, illite, barite, or gorceixite. An alternative path to potassium liberation could
452 be alunite weathering at increasing pH. In this case, another source provides silica in sufficient
453 quantities for opal precipitation. This seems unlikely because illite and K-feldspar formation, at the
454 expense of alunite, remove silica from solution.

455 The association of alunite, kaolinite, illite, and K-feldspar might serve as a tracer for the solution
456 composition as it indicates large variations of pH and silica concentration (Raymahashay 1968). The
457 co-occurrence of opal-A with opal-CT, chalcedony, and quartz also suggests that the silica
458 concentration in solution varied significantly. The kaolinite-alunite-opal assemblage is common in
459 Australian opal deposits (Jones et al. 1966; Bird et al. 1990; Barnes et al. 1992) and is reported for
460 weathering profiles associated with the action of acidic sulfurous solutions on clay minerals and mica
461 (McArthur et al. 1991; Blanco et al. 2008; Wray 2011). Extensive replacement of kaolinite by alunite in
462 the Andamooka host rock implies such an acidic environment in which silica is solubilized and leached
463 from the deeply weathered mudstone. Alunite forms at $pH < 5.5$ whenever sufficient quantities of sulfur,
464 potassium and aluminum are available (Raymahashay 1968). Oxidation of the cretaceous dark colored,

465 pyritic claystone below the opal level (Carr et al. 1979; Alexander et al. 2006) could release necessary
466 sulfur and induce a pH drop. As ferrolysis is the most likely cause of groundwater acidification in
467 inland Australia (McArthur et al. 1991; Thiry et al. 2006), impregnations by iron oxides at Andamooka
468 and the formation of iron concretions at Yowah could be remnants of this process. At 25 °C, the
469 kaolinite-alunite conversion requires a pH ~5 at quartz saturation and ~3.7 at amorphous silica
470 saturation (Raymahashay 1968; Fig. 10a). It is therefore likely that uniform spheres with low Na/K
471 formed during episodes of alunite precipitation at pH <3.7. Bird et al. (1990) measured a K-Ar age of
472 8.4 ± 0.1 Ma obtained from alunite in the Andamooka precious opal field, and concluded that alunite is
473 a late-stage product of Late Miocene weathering. This might indicate that monodisperse spheres with
474 low Na/K are of the same age.

475 **Formation of uniform spheres at proposed acidic pH**

476 Opal-A and alunite can co-precipitate at pH <3.7. This pH region comprises the isoelectric point
477 (IEP) of amorphous silica, where the solubility of amorphous silica and stability of colloidal silica
478 exhibit a local maximum (Fig. 10b). Differences between Na and K cations, with respect to aggregation
479 kinetics, are not to be expected (Wijnen et al. 1993). At the IEP, sphere aggregation is slowed down
480 even at high ionic strengths (Kobayashi et al. 2005). Additionally, experimental work on geothermal
481 brine solutions demonstrated a significant decrease in silica precipitation at pH ~4 compared to pH 7.5-
482 9 (Rothbaum et al. 1979) and pronounced silica nanocolloid stability at low pH regardless of ionic
483 strength (Conrad et al. 2007). These relationships could possibly explain the absence of a correlation
484 between opal type and total impurity level.

485 Numerous authors have pointed to the existence of stable silica colloids at alkaline conditions
486 only, in order to estimate the pH at precious opal formation (e.g., Williams and Crerar 1985; Brown et
487 al. 2004; Rey 2013) based on the relation between pH and silica sol formation given by Iler (1979).
488 However, the complete reference (Iler 1979, p. 366) states that at pH 8-10, sols are only generally
489 stable in the absence of salts. In this context, it should be noted that natural opal-A develops from

490 siliceous fluids with a complex ion composition, which are subject to evaporation and probably
491 significant changes of the ionic strength. This salinity relation is an important aspect that needs to be
492 taken critically when synthetic and natural silica colloid formation is compared.

493 In a broader geological picture it is commonly assumed that precious opal precipitation requires a
494 two-step mechanism occurring at all present opal fields in all local environments. The first step
495 involves the dissolution of feldspar, mica, and clay minerals at low pH and the second step involves
496 silica precipitation at high pH. It seems easier to assume co-formation of all major phases near the IEP
497 of silica without calling for coeval regional and local changes in pH in large areas (e.g., Rey 2013). We
498 propose that slow sphere aggregation could proceed at acidic pH, favoring the growth of monodisperse
499 spheres with repulsive forces large enough to keep them separated in solution, and to arrange them in
500 an ordered array prior to the evaporation of interstitial fluids. On the other hand, polydisperse spheres
501 probably formed at conditions associated with higher pH and different anion composition, resulting in
502 lower amorphous silica solubility, unstable nuclei, or fast aggregation due to lower repulsive
503 interparticle forces. The absence of Na-rich minerals from the samples precludes drawing firm
504 conclusions about the formation conditions of opal-A with high Na/K based on the associated mineral
505 assemblage.

506

507

IMPLICATIONS

508 While the conditions discussed apply to Andamooka and Yowah opal-A, the formation of stable
509 uniformly sized silica spheres at acidic conditions can probably be generalized to other sedimentary
510 precious opal deposits. In Australia, the major economically important opal fields lie in the Great
511 Artesian Basin and display systematic geological and mineralogical similarities (Barnes et al. 1992;
512 Landgrebe et al. 2013). They all contain silcretes and abundant sulfate minerals such as alunite and
513 gypsum (Jones et al. 1966; Senior et al. 1977; Thiry et al. 2006). Thus, the geochemical signature of
514 opal-A essentially needs to be complemented with that of its host rock and associated minerals, as they

515 record the complex history of opal-forming solutions. In order to achieve this goal, it is mandatory to
516 combine a quantitative opal classification, decoupled from gemological properties, with accurate
517 microanalyses able to distinguish between closely spaced opals and to avoid contamination with
518 mineral inclusions.

519 Based on high-resolution measurements of opals and associated minerals combined with colloid-
520 chemical models from materials science, new insights into the formation and evolution of nanocolloidal
521 silica in natural aqueous systems may be generated. The investigation of opal-A micromorphology and
522 -chemistry may also reveal clues for the understanding of structural and chemical reorganization
523 mechanisms behind silica pseudomorphism. Indeed, further detailed studies that include local analysis
524 of mineral chemistry, structure, and association are necessary to restrict the physico-chemical
525 environment in which opal-A forms. Due to the wide distribution of amorphous silica as a weathering
526 product and cementing agent in a variety of geologically important settings on earth's surface and
527 subsurface, being a potential precursor for crystalline silica, the formation of natural silica spheres
528 awaits elucidation.

529

530

ACKNOWLEDGMENTS

531 We thank Jürgen Ganzel (Berlin) for supplying the opal samples from Andamooka and Yowah.
532 The Associate Editor (Maarten Broekmans) and Eloïse Gaillou are sincerely thanked for their detailed
533 and thoughtful comments. We thank Tom Grant for final language editing.

534

535

REFERENCES CITED

536 Abràmoff, M.D., Magalhães, P.J., and Ram, S.J. (2004) Image processing with ImageJ. Biophotonics
537 International, 11, 36–42.

- 538 Alexander, G.B., Heston, W.M., and Iler, R.K. (1954) The solubility of amorphous silica in water.
539 *Journal of Physical Chemistry*, 58, 453–455.
- 540 Alexander, E.M., Sansome, A., and Cotton, T.B. (2006) Eromanga Basin - Lithostratigraphy and
541 environments of deposition. In Cotton, T.B., Scardigno, M.F., and Hibburt, J.E., Eds., *The Petroleum*
542 *Geology of South Australia*, Vol. 2, p. 148-166. Department of Primary Industries and Resources,
543 Government of South Australia.
- 544 Barnes, L.C., Townsend, I.J., Robertson, R.S., and Scott, D.C., Eds. (1992) *Opal: South Australia's*
545 *gemstone*, 176 p. Handbook No. 5, Department of Mines and Energy, Geological Survey of South
546 Australia.
- 547 Bayliss, P. and Males, P.A. (1965) The mineralogical similarity of precious and common opal from
548 Australia. *Mineralogical Magazine*, 35, 429–431.
- 549 Bird, M.I, Chivas, A.R., and McDougall, I. (1990) An isotopic study of surficial alunite in Australia 2.
550 Potassium-argon geochronology. *Chemical Geology*, 80, 133–145.
- 551 Blanco, J.A., Armenteros, I., and Huerta, P. (2008) Silcrete and alunite genesis in alluvial palaeosols
552 (late Cretaceous to early Palaeocene, Duero basin, Spain). *Sedimentary Geology*, 211, 1–11.
- 553 Bogush, G.H. and Zukoski, C.V. (1991) Uniform silica particle precipitation: an aggregative growth
554 model. *Journal of Colloid and Interface Science*, 142, 19–34.
- 555 Brown, L.D., Ray, A.S., and Thomas, P.S. (2004) Elemental analysis of Australian amorphous banded
556 opals by laser-ablation ICP–MS. *Neues Jahrbuch für Mineralogie Monatshefte*, 9, 411-424.
- 557 Carr, S.G., Olliver, J.G., Connor, C.H.H., and Scott, D.C. (1979) Andamooka opal fields: The geology of
558 the precious stones field and the results of the subsidised mining program, 68 p. Report of
559 Investigations 51, Department of Mines and Energy, Geological Survey of South Australia.

- 560 Conrad, C.F., Icopini, G.A., Yasuhara, H., Bandstra, J.Z., Brantley, S.L., and Heaney, P.J. (2007)
561 Modeling the kinetics of silica nanocolloid formation and precipitation in geologically relevant aqueous
562 solutions. *Geochimica et Cosmochimica Acta*, 71, 531–542.
- 563 Crerar, D.A., Axtmann, E.V., and Axtmann, R.C. (1981) Growth and ripening of silica polymers in
564 aqueous solutions. *Geochimica et Cosmochimica Acta*, 45, 1259–1266.
- 565 Darragh, P.J., Gaskin, A.J., Terrell, B.C., and Sanders, J.V. (1966) Origin of precious opal. *Nature*, 209,
566 13–16.
- 567 Dill, H.G. (2001) The geology of aluminum phosphates and sulphates of the alunite group minerals: a
568 review. *Earth-Science Reviews*, 53, 35–93.
- 569 Dove, P.M. and Craven, C.M. (2005) Surface charge density on silica in alkali and alkaline earth
570 chloride electrolyte solutions. *Geochimica et Cosmochimica Acta*, 69, 4963–4970.
- 571 Fitzpatrick, R.W. and Schwertmann, U. (1982) Al-substituted goethite - An indicator of pedogenic and
572 other weathering environments in South Africa. *Geoderma*, 27, 335–347.
- 573 Flörke, O.W. (1955) Zur Frage des “Hoch”-Cristobalit in Opalen, Bentoniten und Gläsern. *Neues*
574 *Jahrbuch für Mineralogie Monatshefte*, 10, 217–224.
- 575 Flörke, O.W., Hollmann, R., Rad, U.v., and Rösch, H. (1976) Intergrowth and twinning in opal-CT
576 lepispheres. *Contributions to Mineralogy and Petrology*, 58, 235–242.
- 577 Gaillou, E., Delaunay, A., Rondeau, B., Bouhnik-le-Coz, M., Fritsch, E., Cornen, G., and Monnier, C.
578 (2008a) The geochemistry of gem opals as evidence of their origin. *Ore Geology Reviews*, 34, 113–
579 126.
- 580 Gaillou, E., Fritsch, E., Aguilar-Reyes, B., Rondeau, B., Post, J., Barreau, A., and Ostroumov, M.
581 (2008b) Common gem opal: An investigation of micro- to nano-structure. *American Mineralogist*, 93,
582 1865–1873.

- 583 Ghisoli, C., Caucia, F., and Marinoni, L. (2010) XRPD patterns of opals: A brief review and new results
584 from recent studies. *Powder Diffraction*, 25, 274–282.
- 585 Icopini, G.A., Brantley, S.L., and Heaney, P.J. (2005) Kinetics of silica oligomerization and nanocolloid
586 formation as a function of pH and ionic strength at 25°C. *Geochimica et Cosmochimica Acta*, 69, 293-
587 303.
- 588 Iler, R.K. (1965) Formation of precious opal. *Nature*, 207, 472–473.
- 589 Iler, R.K. (1979) *The chemistry of silica: Solubility, polymerization, colloid and surface properties, and*
590 *biochemistry*, 866 p. Wiley, New York.
- 591 Jones, J.B. and Segnit, E.R. (1971) The nature of opal I. Nomenclature and constituent phases. *Journal*
592 *of the Geological Society of Australia*, 18, 37–41.
- 593 Jones, J.B., Sanders, J.V., and Segnit, E.R. (1964) Structure of opal. *Nature*, 204, 990–991.
- 594 Jones, J.B., Biddle, J., and Segnit, E.R. (1966) Opal genesis. *Nature*, 210, 1353–1354.
- 595 Kobayashi, M., Juillerat, F., Galletto, P., Bowen, P., and Borkovec, M. (2005) Aggregation and
596 charging of colloidal silica particles: effect of particle size. *Langmuir*, 21, 5761–5769.
- 597 Landgrebe, T.C.W., Merdith, A., Dutkiewicz, A., and Müller, R.D. (2013) Relationships between
598 palaeogeography and opal occurrence in Australia: A data-mining approach. *Computers &*
599 *Geosciences*, 56, 76–82.
- 600 Lynne, B.Y., Campbell, K.A., Moore, J.N., and Browne, P.R.L. (2005) Diagenesis of 1900-year-old
601 siliceous sinter (opal-A to quartz) at Opal Mound, Roosevelt Hot Springs, Utah, U.S.A. *Sedimentary*
602 *Geology*, 179, 249–278.
- 603 Marshall, W.L. and Warakowski, J.M. (1980) Amorphous silica solubilities-II. Effect of aqueous salt
604 solutions at 25°C. *Geochimica et Cosmochimica Acta*, 44, 915-924.

- 605 McArthur, J.M., Turner, J.V., and Lyons, W.B. (1991) Hydrochemistry on the Yilgarn Block, Western
606 Australia: Ferrollysis and mineralisation in acidic brines. *Geochimica et Cosmochimica Acta*, 55, 1273–
607 1288.
- 608 McOrist, G.D. and Smallwood, A. (1997) Trace elements in precious and common opals using neutron
609 activation analysis. *Journal of Radioanalytical and Nuclear Chemistry*, 223, 9–15.
- 610 Morgan, G.B. and London, D. (2005) Effect of current density on the electron microprobe analysis of
611 alkali aluminosilicate glasses. *American Mineralogist*, 90, 1131-1138.
- 612 Parker, R.L. (1962) Isomorphous substitution in natural and synthetic alunite. *American Mineralogist*,
613 47, 127-136.
- 614 Piret, F. and Su, B.-L. (2008) Effects of pH and ionic strength on the self-assembly of silica colloids to
615 opaline photonic structures. *Chemical Physics Letters*, 457, 376–380.
- 616 Raymahashay, B.C. (1968) A geochemical study of rock alteration by hot springs in the Paint Pot Hill
617 area, Yellowstone Park. *Geochimica et Cosmochimica Acta*, 32, 499–522.
- 618 Rey, P.F. (2013) Opalisation of the Great Artesian Basin (central Australia): an Australian story with a
619 Martian twist. *Australian Journal of Earth Sciences*, 60, 291-314.
- 620 Rothbaum, H., Anderton, B., Harrison, R., Rohde, A., and Slatter, A. (1979) Effect of silica
621 polymerisation and pH on geothermal scaling. *Geothermics*, 8, 1–20.
- 622 Sanders, J.V. (1964) Colour of precious opal. *Nature*, 204, 1151–1153.
- 623 Schulze, D.G. (1984) The influence of aluminum on iron oxides. VIII. Unit-cell dimensions of Al-
624 substituted goethites and estimation of Al from them. *Clays and Clay Minerals*, 32, 36–44.

- 625 Senior, B.R., McColl, D.H., Long, B.E., and Whiteley, R.J. (1977) The geology and magnetic
626 characteristics of precious opal deposits, southwest Queensland. BMR Journal of Australian Geology &
627 Geophysics, 2, 241–251.
- 628 Sonnefeld, J., Göbel, A., and Vogelsberger, W. (1995) Surface charge density on spherical silica
629 particles in aqueous alkali chloride solutions. Part 1. Experimental results. Colloid and Polymer
630 Science, 273, 926–931.
- 631 Stewart, A.M., Chadderton, L.T., and Senior, B.R. (2010) Self-assembly in the growth of precious opal.
632 Journal of Crystal Growth, 312, 391–396.
- 633 Thiry, M., Milnes, A.R., Rayot, V., and Simon-Coinçon, S. (2006) Interpretation of palaeoweathering
634 features and successive silicifications in the Tertiary regolith of Inland Australia. Journal of the
635 Geological Society of London, 163, 723–736.
- 636 Webb, J.A. and Finlayson, B.L. (1987) Incorporation of Al, Mg, and water in opal-A: Evidence from
637 speleothems. American Mineralogist, 72, 1204–1210.
- 638 Whitney, D.L. and Evans, B.W. (2010) Abbreviations for names of rock-forming minerals. American
639 Mineralogist, 95, 185–187.
- 640 Wijnen, P.W.J.G, Beelen, T.P.M., Rummens, K.P.J., and van Santen, R.A. (1993) The role of cations in
641 the formation of aqueous silica gels. Journal of Non-Crystalline Solids, 152, 127–136.
- 642 Williams, L. and Crerar, D. (1985) Silica diagenesis, II. General mechanisms. Journal of Sedimentary
643 Petrology, 55, 312–321.
- 644 Wray, R.A.L. (2011) Alunite formation within silica stalactites from the Sydney Region, South-eastern
645 Australia. International Journal of Speleology, 40, 109–116.
- 646 Xia, Y., Gates, B., Yin, Y., and Lu, Y. (2000) Monodispersed colloidal spheres: old materials with new
647 applications. Advanced Materials, 12, 693–713.

Figure captions

648

649 **Figure 1.** Photographs of raw, unprepared sample materials from Andamooka and an ironstone nodule
650 from Yowah.

651 **Figure 2.** Thin section micrographs of microstructural and texture aspects of silicified samples. **(a)** A
652 kaolinite-quartz band with patches of light brown opal (A) within a silty mudstone from Andamooka.
653 Transparent opal (B) intruded and deformed the clay-rich band and light brown opal. **(b)** Partially
654 dissolved rhombic pseudomorphs in the silicified pebble from Andamooka. The cavity walls are lined
655 with translucent, botryoidal silica aggregates. **(c)** A rhombic opal-A pseudomorph embedded in the
656 goethite groundmass of a Yowah ironstone nodule. **(d)** White opal-A from Andamooka with numerous
657 illite-filled polygonal desiccation cracks.

658 **Figure 3.** BSE images (except c) of mineral associations in the host rock and silicified sediments. **(a)**
659 The deeply weathered Andamooka host rock with alunite (Alu), kaolinite (Kln), and quartz (Qz) in
660 their typical spatial context. **(b)** Kaolinite (dark gray) next to illite (white) with kaolinitized lamellae,
661 surrounded by transparent opal-A within a silty mudstone from Andamooka. **(c)** Photomicrograph of an
662 altered K-feldspar grain (center) in direct contact with deformed ooid-like, concentric particles within
663 the opal breccia from Andamooka. **(d)** A gorceixite-florencite-(Ce) rim lining a pore left by grain-
664 dissolution. The rim is surrounded by transparent opal-A within the opal breccia from Andamooka.
665 Gray level differences are related to Ba - Ce substitution.

666 **Figure 4.** SEM images of characteristic appearances of opal-A (a-d) and opal-CT (e and f) after HF
667 etching (except b and c). Scale bar in all images is 1 μm . **(a)** Transparent opal with blue POC from
668 Andamooka, consisting of uniform, well-ordered spheres. Several spheres show a central
669 20-50 nm-sized nucleus or depression (arrows). **(b)** White opal without POC from Andamooka,
670 composed of intersecting polydisperse spheres coated with a thin layer of silica cement. **(c)** Translucent

671 white opal replacing a mollusc shell from Andamooka. The deformed, uniform, and well-ordered
672 spheres have a hexagonal shape. **(d)** Elongated spheres in a narrow goethite-lined vein in a Yowah
673 ironstone nodule. Some stretched particles contain open pores (arrows). **(e)** A detailed view of
674 well-bladed lepispheres ($\sim 30 \mu\text{m}$ across) lining a partly dissolved quartz surface in the silicified pebble
675 from Andamooka. The lepispheres consist of intergrown $\sim 60 \text{ nm}$ thick platelets with jagged edges that
676 resemble aligned silica spheres. **(f)** Poorly bladed, ellipsoidal lepispheres in a cavity located $\sim 200 \mu\text{m}$
677 from (e). The platelets consist of 60-120 nm large silica nanospheres and are notably thicker and
678 shorter than in well-bladed lepispheres.

679 **Figure 5.** Sphere size distribution in opal-A. The relative standard deviation (in %) versus the average
680 sphere diameter (in nm) reveals a division into monodisperse and polydisperse spheres.

681 **Figure 6.** BSE image of a typical location for electron probe microanalysis of white opal-A with
682 desiccation cracks (left) and transparent opal-A (right).

683 **Figure 7.** The sum of Na and K (in wt%) versus the Na/K ratio of polydisperse and monodisperse
684 spheres. Error bars represent $\pm 1\sigma$ of measurements.

685 **Figure 8.** Typical diffractograms of opal-A (lower graph) and the opal breccia containing opal-CT
686 (upper graph). Diffractograms are shifted for clarity. All opal-A samples display a characteristic broad
687 reflection at $\sim 22.2^\circ 2\theta$. Quartz impurities (Qz) in the opal breccia originate from quartz cement
688 between the clasts. The major peaks at ~ 21.7 and $\sim 35.9^\circ 2\theta$ are indicative of opal-CT.

689 **Figure 9.** The correlation between the sum of mono- and divalent cations (Na + K + Ca + Sr + Ba +
690 Mg + Mn) and trivalent cations (Al + Fe³⁺) in opal-A from Andamooka and Yowah. Andamooka opal
691 compositions from Bayliss and Males (1965) and Brown et al. (2004) are plotted for comparison. A
692 data point from Gaillou et al. (2008a) is located at $\sim (1.00; 0.77)$ but was excluded from the plot for
693 legibility.

694 **Figure 10. (a)** Stability fields of gibbsite, kaolinite, muscovite, K-feldspar, and natural alunite as a
 695 function of pH and silica concentration at ambient conditions (after Raymahashay 1968). **(b)** Effects of
 696 pH and salinity on the colloid stability in the amorphous silica-water system (after Iler 1979).

697

698

Tables

699 **Table 1.** Sample characteristics of silicified sediments, opals, and the unsilicified host rock in this
 700 study.

Locality	Sample type	Opal-A type	Opal-A color	Associated minerals identified ^a	
				Major constituents	Accessory constituents
Andamooka	mudstone (host rock)	-	-	Kln, Qz, Alu,	Ill, Hem, Ant, Brt
	silty mudstone	C/P	white, light brown, colorless, transparent honey-colored	Kln, Qz	Ill, Ant, Brt, Hem, Alu, Kfs, Gp
	conglomerate with clay matrix	C/P	white, light brown, colorless, transparent honey-colored	Kln, Qz	Ill, Hem, Ant, Alu, Brt, Kfs, Gp
	opal breccia	C/P	colorless	Opl-CT, Qz	Kln, Ill, Brt, Kfs, Alu, Hem, Ant, Cha, Gp, Gcx, Gcx-Flc
	grey pebble	P	transparent	Qz	Opl-CT, Ill, Brt
	mollusc shells	P	translucent white, grey	-	-
	coniferous wood	C/P	white, colorless, transparent honey-colored	-	Kln, Ant
			colorless	Gth, Hem, Kln	Ill, Ant, Kfs, Gz

Notes: a - Mineral abbreviations after Whitney and Evans (2010).

Other abbreviations used: C - common opal; P - precious opal; Cha - chalcedony; Flc - florencite; Gcx - gorceixite; Gz - goyazite.

701

702 **Table 2.** Representative chemical analyses of opal-A samples by EPMA (given in wt%).

oxide	Andamooka opal-A			Yowah opal-A	
	poly	mono	shells	mono	pseud
Na ₂ O	0.13	0.10	0.17	0.09	0.08
K ₂ O	0.03	0.12	0.15	0.18	0.14
MgO	0.03	0.01	0.03	0.02	0.02
CaO	0.06	0.05	0.40	0.09	0.07
SrO	<LLD	<LLD	<LLD	0.01	<LLD
BaO	0.02	0.03	0.02	0.02	0.02
MnO	0.01	0.01	0.02	0.01	0.01
Fe ₂ O ₃ -total	0.12	0.07	0.05	0.21	0.03
Al ₂ O ₃	0.96	0.89	1.53	0.89	0.75
TiO ₂	0.02	0.01	0.02	0.01	0.01
SiO ₂	93.21	90.90	89.40	92.66	92.54
SUM total	94.59	92.20	91.79	94.19	93.67
SUM impurities	1.38	1.31	2.39	1.52	1.13
calculated values					
(H ₂ O + OH) ^a	5.41	7.80	8.21	5.81	6.33
Na + K	0.06	0.09	0.12	0.11	0.09
Na/K	4.16	0.70	0.98	0.45	0.49

Notes: Abbreviations: poly - polydisperse; mono - monodisperse; shells - monodisperse spheres in mollusc shells; pseud - monodisperse spheres in rhombic pseudomorphs.

a - Calculated by balance of SUM total with 100 wt%.

703

704

705

706

707

708

709

710

711 **Table 3.** Representative chemical analyses of opal-associated minerals from the Andamooka and
 712 Yowah precious opal fields by EPMA (given in wt%).

oxide	Andamooka							Yowah			
	Kln	lIt	Kfs	Alu host	Alu silic.	Gcx ^b	Gcx-Flc ^c	Kln	lIt	Kfs	Gz
Na ₂ O	<LLD	0.63	0.47	0.48	0.77	0.14	0.23	<LLD	0.09	0.82	0.17
K ₂ O	0.06	6.82	16.14	10.13	7.94	0.12	0.09	0.16	6.15	15.52	4.27
MgO	0.03	1.47	0.01	0.04	0.04	0.02	<LLD	0.11	1.27	<LLD	0.03
CaO	0.07	0.27	0.01	0.09	0.24	0.76	1.51	0.08	1.01	<LLD	1.52
SrO	<LLD	<LLD	<LLD	0.02	0.92	0.69	1.30	<LLD	<LLD	<LLD	6.89
BaO	<LLD	<LLD	0.24	0.13	3.64	23.70	14.39	<LLD	<LLD	0.26	3.61
MnO	0.01	<LLD	0.02	0.03	0.01	0.02	<LLD	<LLD	<LLD	0.02	0.16
Fe ₂ O ₃ -total	1.50	2.94	0.03	4.27	3.70	0.84	1.09	2.84	3.65	0.06	11.39
Al ₂ O ₃	37.81	29.21	18.26	33.43	33.24	29.88	30.23	37.13	28.86	18.20	26.16
TiO ₂	0.02	0.29	0.02	<LLD	0.02	0.04	0.03	0.04	0.09	0.03	0.05
SiO ₂	46.65	50.34	64.68	0.19	1.11	0.88	0.29	45.93	52.50	64.34	0.87
P ₂ O ₅	<LLD	<LLD	<LLD	0.32	1.91	26.60	28.16	<LLD	<LLD	<LLD	19.40
SO ₃	<LLD	<LLD	<LLD	37.87	33.62	0.89	0.71	<LLD	<LLD	<LLD	11.53
LREE ₂ O ₃ ^a	<LLD	<LLD	<LLD	<LLD	0.13	2.63	9.06	<LLD	<LLD	<LLD	0.10
SUM total	86.13	91.96	99.86	86.99	87.26	87.21	87.08	86.29	93.61	99.24	86.13

Notes: Alunite in the non-silicified host rock is labeled "Alu host". Alunite in silicified sediments is labeled "Alu silic.".

a - LREE₂O₃ is the sum of La, Ce, Pr, and Nd oxides.

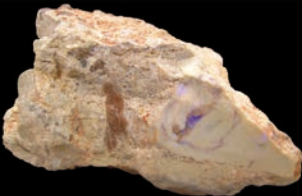
b - LREE₂O₃ in Gcx (in wt%): La₂O₃ 0.21, Ce₂O₃ 1.86, Pr₂O₃ 0.10, and Nd₂O₃ 0.46.

c - LREE₂O₃ in Gcx-Flc (in wt%): La₂O₃ 0.46, Ce₂O₃ 7.35, Pr₂O₃ 0.23, and Nd₂O₃ 1.02.

713

Figure 1

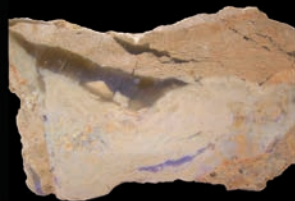
conglomerate



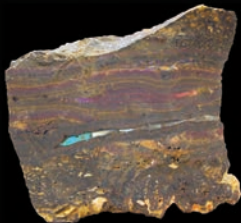
opal breccia



silty mudstone



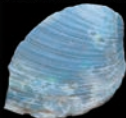
ironstone nodule



coniferous wood



mollusc shell



1 cm

Figure 2

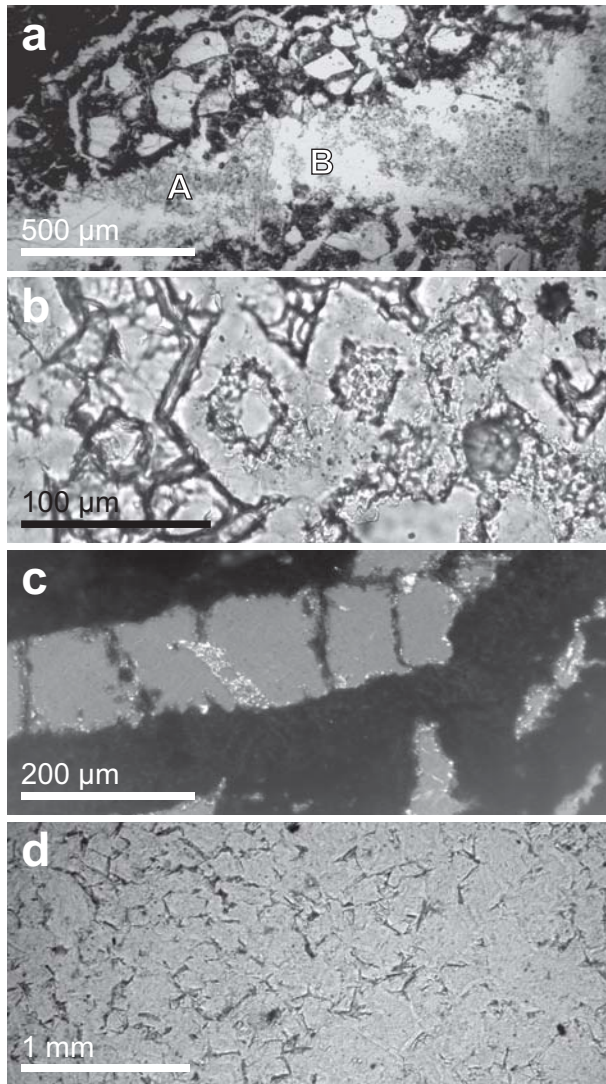


Figure 3

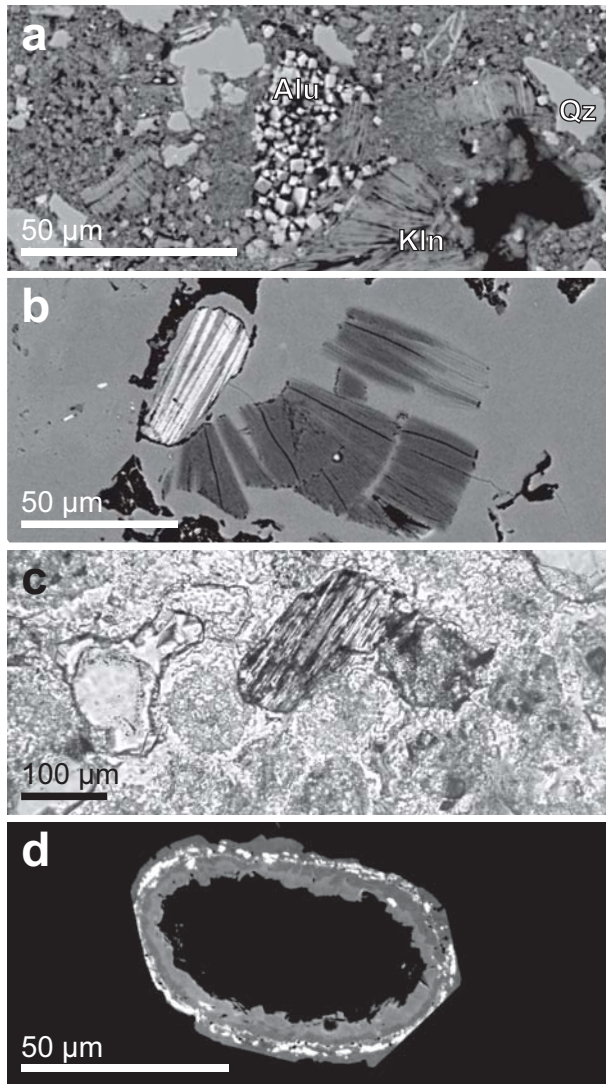


Figure 4

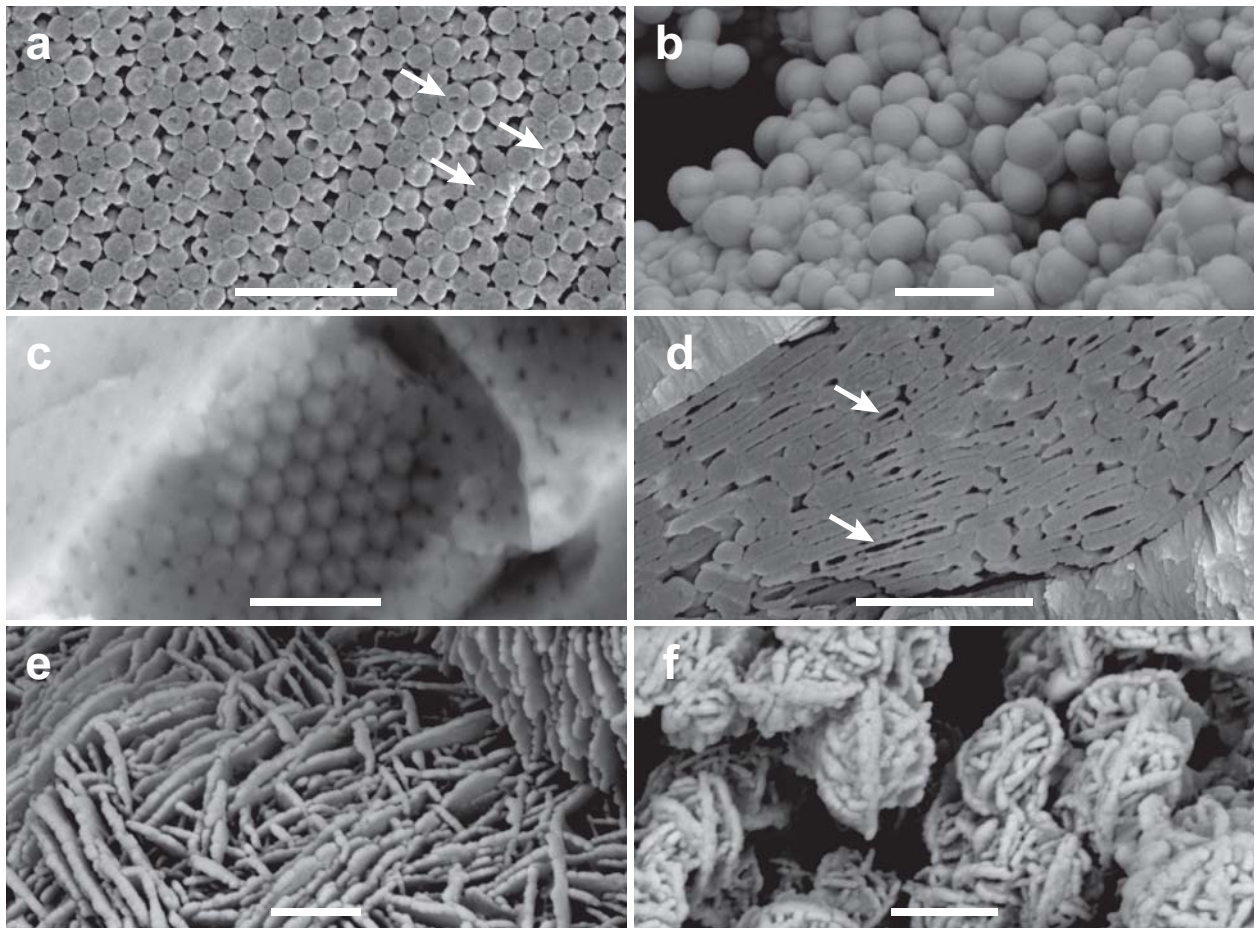


Figure 5

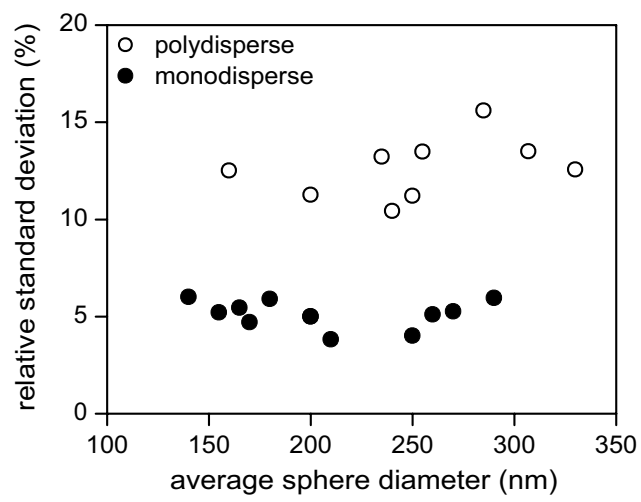


Figure 6

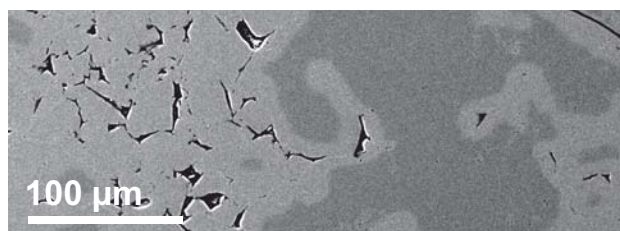


Figure 7

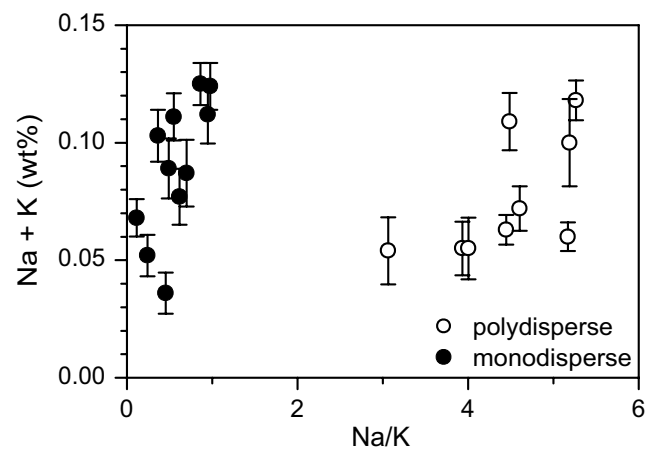


Figure 8

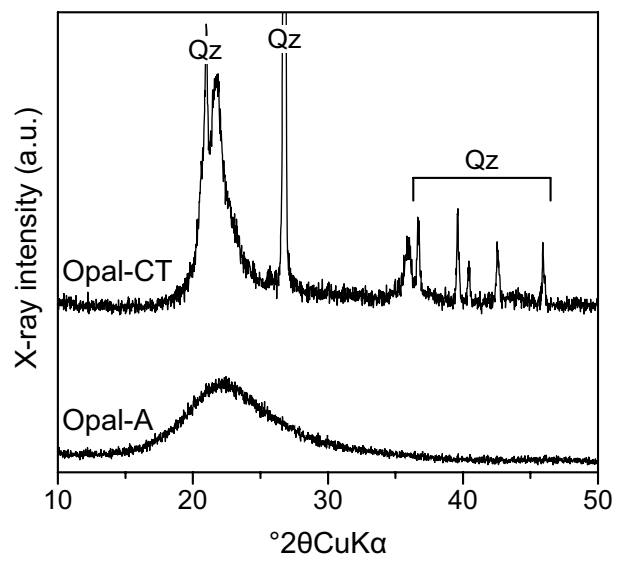


Figure 9

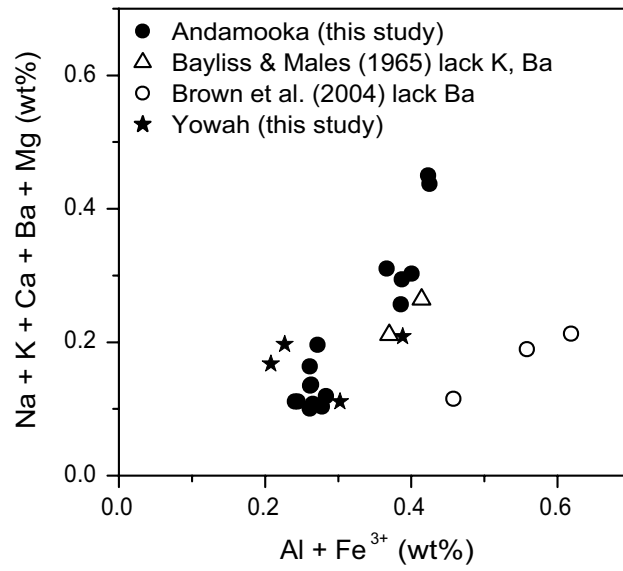


Figure 10

